

## Communication

## Ultrasensitive Three-Dimensional Orientation Imaging of Single Molecules on Plasmonic Nanohole Arrays using Second Harmonic Generation

Sushant P Sahu, Amirreza Mahigir, Benjamin Chidester, Georgios Veronis, and Manas Ranjan Gartia

*Nano Lett.*, **Just Accepted Manuscript** • DOI: 10.1021/acs.nanolett.9b02239 • Publication Date (Web): 07 Aug 2019

Downloaded from [pubs.acs.org](https://pubs.acs.org) on August 9, 2019

### Just Accepted

“Just Accepted” manuscripts have been peer-reviewed and accepted for publication. They are posted online prior to technical editing, formatting for publication and author proofing. The American Chemical Society provides “Just Accepted” as a service to the research community to expedite the dissemination of scientific material as soon as possible after acceptance. “Just Accepted” manuscripts appear in full in PDF format accompanied by an HTML abstract. “Just Accepted” manuscripts have been fully peer reviewed, but should not be considered the official version of record. They are citable by the Digital Object Identifier (DOI®). “Just Accepted” is an optional service offered to authors. Therefore, the “Just Accepted” Web site may not include all articles that will be published in the journal. After a manuscript is technically edited and formatted, it will be removed from the “Just Accepted” Web site and published as an ASAP article. Note that technical editing may introduce minor changes to the manuscript text and/or graphics which could affect content, and all legal disclaimers and ethical guidelines that apply to the journal pertain. ACS cannot be held responsible for errors or consequences arising from the use of information contained in these “Just Accepted” manuscripts.

# Ultrasensitive Three-Dimensional Orientation Imaging of Single Molecules on Plasmonic Nanohole Arrays using Second Harmonic Generation

*Sushant P. Sahu*<sup>1,†</sup>, *Amirreza Mahigir*<sup>2,3,†</sup>, *Benjamin Chidester*<sup>A</sup>, *Georgios Veronis*<sup>2,3</sup>,  
*Manas Ranjan Gartia*<sup>1, \*</sup>

<sup>1</sup>Department of Mechanical and Industrial Engineering, Louisiana State University, Baton Rouge,  
LA 70803

<sup>2</sup>School of Electrical Engineering and Computer Science, Louisiana State University, Baton  
Rouge, LA 70803

<sup>3</sup>Center for Computation and Technology, Louisiana State University, Baton Rouge, LA 70803

<sup>4</sup>Department of Computational Biology, School of Computer Science, Carnegie Mellon  
University, Pittsburgh, PA 15213

<sup>†</sup>Equal contribution

**KEYWORDS:** Single molecule imaging, SHG, Orientation, Nanohole arrays

## **ABSTRACT**

Recently, fluorescence-based super-resolution techniques such as stimulated emission depletion (STED) and stochastic optical reconstruction microscopy (STORM) have been developed to achieve near molecular scale resolution. However, such a super-resolution technique for nonlinear label-free microscopy based on second harmonic generation (SHG) is lacking. Since SHG is label-free and does not involve real-energy level transitions, fluorescence-based super-resolution

1  
2  
3 techniques such as STED cannot be applied to improve the resolution. In addition, due to the  
4  
5 coherent and non-isotropic emission nature of SHG, single-molecule localization techniques based  
6  
7 on isotropic emission of fluorescent molecule such as STORM will not be appropriate. Single  
8  
9 molecule second harmonic generation microscopy is largely hindered due to the very weak non-  
10  
11 linear optical scattering cross-sections of SHG scattering processes. Thus, enhancing SHG using  
12  
13 plasmonic nanostructures and nanoantennas has recently gained much attention owing to the  
14  
15 potential of various nanoscale geometries to tightly confine electromagnetic fields into small  
16  
17 volumes. This confinement provides substantial enhancement of electromagnetic field in  
18  
19 nanoscale regions of interest, which can significantly boost the nonlinear signal produced by  
20  
21 molecules located in the plasmonic hotspots. However, to date, plasmon-enhanced SHG has been  
22  
23 primarily applied for the measurement of bulk properties of the materials/molecules and single  
24  
25 molecule SHG imaging along with its orientation information has not been realized yet. Herein,  
26  
27 we achieved simultaneous visualization and three-dimensional orientation imaging of individual  
28  
29 Rhodamine 6G (R6G) molecules in the presence of plasmonic silver nanohole arrays. SHG and  
30  
31 two-photon fluorescence microscopy experiments together with finite-difference time-domain  
32  
33 (FDTD) simulations revealed  $\sim 10^6$ -fold nonlinear enhancement factor at the hot spots on the  
34  
35 plasmonic silver nanohole substrate, enabling detection of single molecules using SHG. The  
36  
37 position and 3D orientation of R6G molecules was determined using the template matching  
38  
39 algorithm by comparing the experimental data with the calculated dipole emission images. These  
40  
41 findings could enable SHG-based single molecule detection and orientation imaging of molecules  
42  
43 which could lead to a wide range of applications from nanophotonics to super-resolution SHG  
44  
45 imaging of biological cells and tissues.  
46  
47  
48  
49  
50  
51  
52  
53  
54  
55  
56  
57  
58  
59  
60

## INTRODUCTION

Fluorescence-based super-resolution techniques such as stimulated emission depletion (STED)<sup>1, 2</sup> and photo-activated localization microscopy (Photo-activated localization microscopy: PALM, Fluorescence Photoactivation Localization Microscopy: FPALM, STORM)<sup>3, 4</sup> have been developed to achieve near molecular scale resolution. However, such a super-resolution technique for nonlinear label-free microscopy based on second harmonic generation (SHG) is lacking. Point spread function (PSF) is generally engineered to improve the resolution of a microscopy system. Fluorescence emissions are typically incoherent and the radiation patterns are isotropic. In contrast, SHG emission is coherent and radiation patterns are directional in nature.<sup>5, 6</sup> Therefore, the super-resolution techniques developed for fluorescence microscopy systems are not readily applicable to nonlinear microscopy systems such as SHG.

SHG is a nonlinear coherent optical scattering process usually by non-centrosymmetric systems in which two lower energy photons are up-converted to a single photon with exactly double the incident light energy. The SHG yield grows as the square of the fundamental incident field intensity.<sup>7, 8, 9</sup> Enhancing SHG from plasmonic nanostructures and nanoantennas has recently received a lot of attention owing to the potential of various nanoscale geometries to tightly confine electromagnetic fields into small volumes and provide substantial field enhancement in nanoscale regions of interest.<sup>8, 10-20</sup> The plasmonic resonances from nanostructures have been utilized for multitude of photonic applications including surface-plasmon enhanced nonlinear emission,<sup>10-19</sup> single molecule detection,<sup>21</sup> surface-enhanced Raman scattering,<sup>22,23,24</sup> metal-enhanced photoluminescence,<sup>25,26</sup> plasmon-enhanced sensing,<sup>16</sup> photocatalysis<sup>27</sup>, and optical manipulation of light.<sup>28,29</sup> Thoughtful design and surface engineering of plasmonic nanostructured arrays are able to produce areas called “hot spots” where the induced electromagnetic field intensity is

1  
2  
3 enhanced by several orders of magnitude which can significantly increase the nonlinear signal  
4 produced by a nonlinear material located in plasmonic nanogaps, especially when resonantly  
5 pumped.<sup>20</sup> Plasmonic nanostructures resulting in generation of second harmonic light include gold  
6 nanostars,<sup>30</sup> silver triangular nanoprisms,<sup>31</sup> holes in metallic films,<sup>32</sup> curved nanorods,<sup>33</sup> split-ring  
7 resonators with U-shape,<sup>34</sup> metal-dielectric nanodisks,<sup>35</sup> gold T-dimers,<sup>36</sup> nanocups,<sup>37</sup> chiral G-  
8 shaped nanoparticles,<sup>38</sup> chiral helices,<sup>39</sup> L-shaped nanoparticles<sup>40</sup> and gold nanotips.<sup>41</sup> Previously  
9 we have used nanohole-based plasmonic substrate in the linear optical regime to achieve highly  
10 sensitive colorimetric sensing<sup>23,42</sup> and enhancement of Raman scattering of the order of  $2 \times 10^5$ .<sup>24</sup>  
11 Here, we operate a nanohole array-based substrate in the non-linear optical regime, and  
12 demonstrate highly sensitive single molecule detection and simultaneous 3D orientation mapping  
13 of rhodamine 6G molecules using second harmonic generation microscopy. Determining the  
14 molecular orientation of single molecules is fundamentally important in biophysics to study  
15 conformational changes of biomolecules<sup>43</sup> and/or the rotational motion of molecular motors,<sup>44</sup> in  
16 the analyses of photophysical processes such as Fluorescence Resonance Energy Transfer (FRET)  
17 which are governed by orientation of materials,<sup>45</sup> in molecular nanotechnology,<sup>46</sup> biotechnology<sup>47</sup>  
18 and also in catalysis.<sup>48</sup> Previous methods of determining the 3D dipole orientation of single  
19 fluorescent molecules include: (i) probing the far-field emission pattern through polarization-  
20 resolved microscopy method that rely on excitation and/or emission with multiple  
21 polarizations,<sup>49,50</sup> (ii) observing dipole radiation pattern in defocused wide-field imaging technique  
22 which takes advantage of bright fluorescence properties of dipole emitters as opposed to very weak  
23 non-linear optical cross-sections of processes such as SHG,<sup>51</sup> (iii) direct imaging of pupil  
24 functions,<sup>52</sup> (iv) double-helix point spread function engineering,<sup>53</sup> and (v) using annular  
25 illumination to generate characteristic field distributions.<sup>54</sup> However, similar 3D orientation  
26  
27  
28  
29  
30  
31  
32  
33  
34  
35  
36  
37  
38  
39  
40  
41  
42  
43  
44  
45  
46  
47  
48  
49  
50  
51  
52  
53  
54  
55  
56  
57  
58  
59  
60

1  
2  
3 information with single-molecule resolution has not been obtained using non-linear microscopy  
4 techniques such as SHG.  
5  
6

7  
8 In this letter, we introduce an ultrasensitive collective plasmon enhanced SHG microscopy  
9 method for simultaneous visualization and 3D orientation imaging of individual R6G molecules  
10 using plasmonic silver nanohole arrays. SHG and two-photon fluorescence microscopy  
11 experiments together with numerical simulation results suggest several orders of electromagnetic  
12 field enhancement at the surface hot spots on the plasmonic nanohole substrate compared to R6G  
13 molecules immobilized on a glass substrate, enabling detection of significantly amplified plasmon  
14 enhanced SHG signatures from individual R6G molecules on the plasmonic silver nanohole  
15 structure.  
16  
17  
18  
19  
20  
21  
22  
23  
24  
25

## 26 **RESULTS AND DISCUSSION**

27  
28  
29 The schematic of the experimental set up is shown in Figure 1a. The figure shows the  
30 excitation beam (red) and the collected emitted SHG light (blue) from the molecule on the  
31 plasmonic substrate. For the square nanohole array with pitch (distance between two holes) of 350  
32 nm, a structure with size 1 cm x 1 cm contains about 100 million holes. This provides a unique  
33 platform to perform massively parallel single-molecule imaging. The rationale behind the  
34 nanohole structure is to restrict only a few molecules ( $\sim 0.3$ ) within the confocal volume. In  
35 addition, this geometry minimizes the background and improves the signal-to-noise (SNR) by  
36 preventing the direct excitation of molecules away from the holes due to lower electromagnetic  
37 field intensity outside the holes. The nanohole structure was fabricated by nanoimprint lithography  
38 (*See Methods*). As shown in the AFM image (Figure 1b), the nanoholes are arranged in a square  
39 geometry with hole diameter  $d = 150$  nm, and pitch  $p = 350$  nm. Large area ( $1 \text{ cm}^2$ ) substrates were  
40 fabricated with three different hole depths. The diameter and the pitch were kept constant. The  
41  
42  
43  
44  
45  
46  
47  
48  
49  
50  
51  
52  
53  
54  
55  
56  
57  
58  
59  
60

1  
2  
3 depth of the holes  $h$  was varied between 250 and 1,000 nm. Figures 1c, d, and e show the cross-  
4 sectional scanning electron microscopy (SEM) images of the substrate with three different depths.  
5  
6 The AFM image in Figure 1 and additional top-view SEM images (supplementary information  
7 Figure S1) showed that the designed nanohole arrays exhibit a regular square pattern geometry in  
8 terms of their sizes and shapes.  
9  
10  
11  
12  
13  
14  
15  
16  
17

18 The optical linear resonance spectra of nanohole structures of various geometries and  
19 thicknesses have been discussed in detail in our prior studies.<sup>42</sup> Figure 2a shows the measured SHG  
20 emission spectra of the device with different nanohole depths of 250 nm, 500 nm and 1000 nm,  
21 under a pulsed laser excitation wavelength of 800 nm. The spectra show the SHG peaks at 400  
22 nm, and strong broadband two-photon fluorescence in the range of 425 – 660 nm. Two photon  
23 fluorescence in silver nanostructures is generated due to the transition of electrons from the  $d$ -band  
24 (valence band) to the  $sp$ -band (conduction band). This emitted broadband luminescence is due to  
25 the radiative recombination of electrons and holes after the intraband scattering relaxation of  
26 electrons to the Fermi level.<sup>55</sup> The SHG from the silver nanohole structure is possible because of  
27 the existence of nonzero  $\chi^2$ -value (second-order nonlinear susceptibility) at the silver-polymer and  
28 silver-air interfaces due to the breaking of symmetry of boundary conditions.<sup>36,56</sup> As the inset of  
29 Figure 2a shows, the SHG and two-photon fluorescence signal intensity of the silver nanohole  
30 array increased with increase in the depth of the structure [although the lowest two-photon  
31 fluorescence yield was obtained for the nanohole structure with hole depth of 500 nm (Figure 2  
32 a)]. It is to be noted that the SHG and two photon fluorescence intensities of the nanohole structures  
33 can vary from structure to structure likely due to the inhomogeneous distribution of the apex  
34 dimensions of the nanohole array.<sup>57</sup> To better understand the mechanism behind SHG emission on  
35  
36  
37  
38  
39  
40  
41  
42  
43  
44  
45  
46  
47  
48  
49  
50  
51  
52  
53  
54  
55  
56  
57  
58  
59  
60

1  
2  
3 the plasmonic nanohole structure, finite-difference time-domain (FDTD) simulations<sup>65</sup> were  
4 performed. In order to obtain the second harmonic resonance of the structure, a high-power laser  
5 pulse was used. In our FDTD simulations we use a plane wave at 800 nm wavelength normally  
6 incident on the nanohole array which excites the second harmonic resonance of the structure.  
7  
8 Figure 2b shows the power transmission coefficient of the structure as a function of wavelength in  
9 logarithmic scale. We observe that a second resonance appears at the second harmonic wavelength  
10 of 400 nm in close agreement with our experimental results (Figure 2a). Due to the low two-photon  
11 fluorescence background, a substrate with nanohole depth of 500 nm was chosen for the  
12 subsequent single molecule SHG imaging experiments.

13  
14  
15  
16  
17  
18  
19  
20  
21  
22  
23  
24 To demonstrate single molecule imaging, rhodamine-6G (R6G) dye with a concentration  
25 of 0.25 nM was dispersed on the surface of the plasmonic nanohole structure. First, we want to  
26 provide experimental proof of the presence of the single molecule within the nanohole at that  
27 concentration using fluorescence correlation spectroscopy (FCS).<sup>58</sup> The correlation function in  
28 FCS  $G(\tau) = \langle F(t)F(t + \tau) \rangle / \langle F(t) \rangle^2$  has an inverse relationship with the number of molecules  
29 within the detection volume, where  $\tau$  is the delay (lag) time. Figure 2c indicates that the number  
30 of molecules in the nanohole is smaller compared to the bulk solution based on measurements of  
31 their autocorrelation functions. The inset of Figure 2c shows the raw data of photon counts rate on  
32 the nanohole and bulk solutions. The nanohole structure exhibits about 5x enhancement compared  
33 to the bulk dye solution. The average number of molecules within the nanohole was calculated by  
34 fitting the equation below to the data obtained from fluorescence correlation spectroscopy  
35 experiments<sup>59, 60</sup>

$$G_0 = 1 + \frac{1}{N} \left( 1 - \frac{\langle b \rangle}{\langle i \rangle} \right)^2 (1 + n_r),$$

1  
2  
3 where  $\langle i \rangle$  is the average measured intensity,  $\langle b \rangle$  is the background intensity counts, and  $n_T$  is the  
4  
5  
6 number of molecules in the triplet state, which is 0.35.<sup>67</sup>  $G_0$  is obtained from the function fitted to  
7  
8 autocorrelation data for the nanohole and is found to be  $\sim 4.76$ . Using the data, the average number  
9  
10 of molecules in the nanohole for this particular concentration was found to be  $\sim 0.3$  (*See SI for the*  
11  
12 *calculations*). To get information about the radiative process involved with the enhancement on  
13  
14 the nanohole array structure, fluorescence lifetime experiments were performed. Figure 2d  
15  
16 compares the lifetime of R6G on the nanohole and in bulk solution. The lifetime in bulk was  
17  
18 measured to be 4.035 ns which agrees well with the literature data.<sup>61</sup> The lifetime was decreased  
19  
20 by 6x on the nanohole structure compared to the bulk value. Since the fluorescence lifetime is  $\tau =$   
21  
22  $1/(\Gamma + k_{NR})$ , where  $\Gamma$  is the radiative decay rate, and  $k_{NR}$  is the non-radiative decay rate, and the  
23  
24 quantum yield is  $Q = \Gamma/(\Gamma + k_{NR})$ , we can write  $\Gamma = Q/\tau$ , and  $k_{NR} = (1/\tau) - \Gamma$ . Our experiments  
25  
26 showed decrease of lifetime with increase in quantum yield (Figure 2c and 2d). This indicates that  
27  
28 the enhancement on the nanohole is mainly driven by increase in the radiative decay process.<sup>62</sup>  
29  
30  
31  
32  
33

34 Next, control experiments were performed on the glass substrate without the silver nanohole  
35  
36 substrate. Since the field intensity enhancement is low without any plasmonic nanostructure, 400x  
37  
38 higher concentration of R6G is required on glass to get any detectable signal and such  
39  
40 concentration was employed in our experiments. Both samples (R6G on glass and nanohole  
41  
42 structure) showed two-photon fluorescence in the emission wavelength range of R6G ( $\sim 550$ - $560$   
43  
44 nm) (Figures S5b, S5d). However, only the nanohole plasmonic structure with R6G showed SHG  
45  
46 (Figure S5c). Despite using 400x higher concentration of R6G (10  $\mu\text{M}$ ), the glass substrate did not  
47  
48 show any SHG signal (Figure S5a). The samples on glass showed SHG at R6G concentration of  
49  
50 about 11 mM (Figure S5). Also, we did not observe any detectable SHG on smooth Ag and Au  
51  
52 metal alone (Figure S6) which is expected because of centrosymmetric crystal lattice of the smooth  
53  
54 continuous metal thin films where SHG is forbidden in bulk due to inversion symmetry. R6G  
55  
56 detection on smooth metal substrate was found to be dependent on concentration of R6G dye  
57  
58  
59  
60

1  
2  
3 employed in the experiments with obvious greater sensitivity for detection at higher R6G  
4 concentrations particularly in sub-mM concentration range.  
5  
6

7 Figure 3 presents the single-molecule SHG imaging of R6G within nanoholes, where each  
8 molecule has different orientation. Various patterns were observed with central bright spot with  
9 two full or half Airy ring like structures. It should be noted that the half ring like structures are not  
10 imaging artifacts which we verified by changing the imaging speed and pixel dwelling time.  
11 Furthermore, these are not due to digital photobleaching since SHG should not show any  
12 photobleaching.<sup>63</sup> As seen in Figure 3a, Airy disk emission patterns were visible only for R6G on  
13 the nanohole structures and not on the glass substrate (Figure S5a). Interestingly, some of the  
14 emission patterns also showed half-Airy disk structures that are attributed to different orientation  
15 of R6G molecules on the nanohole substrate. We also note that we did not observe such unique  
16 Airy ring like patterns when imaging the plasmonic silver nanohole structure alone without R6G  
17 dye, where the SHG channel shows weakly emissive dots arising from the silver nanostructures  
18 on the nanohole device (Figure S7). To find the reason for the unique half-Airy ring patterns in the  
19 presence of R6G dye, we calculated the emission pattern of the dipole radiated through the  
20 aperture.<sup>49</sup> Here, we modeled the fluorescence dye as a dipole emitter, and the nanohole as an  
21 aperture. Such calculations were performed closely resembling the nanohole geometry described  
22 at different aperture diameters  $d$ , depths of dipole from the aperture  $z$ , polar angle  $\theta$ , pixel size  $n \times$   
23  $n$ , and azimuthal angle  $\phi$  to generate a library of images (Figures 3c, 4a and SI Figure S8). A total  
24 of 72,000 template images were created for the library. Using the template matching algorithm  
25 (*See Methods and SI for details*), the experimental results were compared with the simulated  
26 library images to find the corresponding  $d$ ,  $z$ ,  $\theta$ ,  $\phi$  by finding the best possible match between a  
27 given image region and the set of library images. It was found that the half-Airy patterns of the  
28 SHG were due to the different orientation of the R6G molecules inside the nanohole. The  
29 experiment and the simulation of the dipole emission patterns through the aperture (nanohole  
30 device) are matched within our angular uncertainty analyses indicating that the molecule (Figure  
31 3b left) has a polar angle  $\theta = 24$  degree, and azimuthal angle  $\phi = 90$ , and is situated at 40 nm from  
32 the surface while the molecule (figure 3b right) is located at 150 nm from the surface having a  
33 polar angle of  $\theta = 30$  degree, and azimuthal angle of  $\phi = 22.5$  degree (Figure 3b, 3c, 3f, 3g). Figure  
34 4a shows the various simulated patterns of single molecules with different orientations at various  
35 aperture depths. The corresponding identified experimental patterns are shown in Figure 4b. The  
36  
37  
38  
39  
40  
41  
42  
43  
44  
45  
46  
47  
48  
49  
50  
51  
52  
53  
54  
55  
56  
57  
58  
59  
60

1  
2  
3 similarity of the patterns for the experimental and simulated images can be clearly observed  
4 confirming the suitability of the algorithm. Furthermore, electromagnetic simulations of the dipole  
5 emission pattern calculated at different polar and azimuthal angles were compared with the z-stack  
6 experimental SHG imaging to recover the orientation angles  $\theta$ ,  $\phi$  of the molecule inside the  
7 plasmonic nanohole structure. Figures 4c and 4d show various SHG emission patterns from R6G  
8 molecules on the plasmonic nanoholes in a larger field of view with many individual molecules at  
9 a single plane. Figure 4e represents 3D mapping of individual R6G molecules obtained from the  
10 z-stack of images. The purpose of Figure 4e was to demonstrate the optical sectioning capability  
11 of multiphoton nonlinear SHG microscopy with 3D orientation mapping by imaging through  
12 sequential z- slices through collection of a z-stack of images. The location of the molecules are  
13 shown as blue dots and the resultant vector angles of  $\theta$  and  $\phi$  are denoted by the red arrows for 31  
14 molecules imaged. This is the first demonstration of highly sensitive simultaneous visualization  
15 and 3D orientation extraction of individual R6G molecules using label-free SHG imaging on  
16 plasmonic nanohole arrays. Figures 4f and 4g show the histogram distribution of extracted  
17 orientation angles  $\theta$ ,  $\phi$  from SHG images. It should be noted that when we include large number  
18 of molecular images ( $\sim 150$  molecules and see *supporting information* Figure S12) in our analysis,  
19 the azimuthal angle ( $\phi$ ) distribution is relatively flat, which means that molecules can be found  
20 with almost equal probability in any  $\phi$  angle ranging from 0 to 360°. The observed SHG emissions  
21 results in Figure S12 show that the most probable orientation of molecules in terms of polar angle  
22 is at  $\theta = 60-70^\circ$  which agrees well with the literature values.<sup>64,65</sup> It should be noted that for  
23 unambiguous detection of molecules, the outer rim of the pattern is very helpful. Therefore, for  
24 precise analysis of orientation angles, the ideal separation between molecules is determined to be  
25  $\sim 1.0 - 1.5 \mu\text{m}$ . Figure 4d depicts the fitted experimentally obtained SHG emission patterns using  
26 the template matching algorithm to obtain both out-of-plane and in-plane-orientation angles  $\theta$ ,  $\phi$ ,  
27 demonstrating that emission from single molecules matches the one of dipole emitters. However,  
28 we also note that it becomes progressively harder to distinguish patterns with an out-of-plane angle  
29 of less than  $30^\circ$ , especially for images with poor signal-to-noise ratio. The image analysis of  
30 Figures 3 and 4 shows that the algorithm performs well for relatively non-overlapping molecular  
31 orientation patterns, even with poor signal to noise counts. Our analysis showed that, if the polar  
32 angle of orientation for the two molecules are between  $\theta = 0 - 30$  degrees, we will likely not be  
33 able to resolve it, though we can still produce some estimate. However, our theoretical templates  
34  
35  
36  
37  
38  
39  
40  
41  
42  
43  
44  
45  
46  
47  
48  
49  
50  
51  
52  
53  
54  
55  
56  
57  
58  
59  
60

sample the possible values of  $\theta = 6^\circ$  and  $\phi = 6^\circ$  using the template matching algorithm employed. So, though our theoretical resolution is 6 degrees, in reality, our ability to resolve angles depends highly upon  $\theta$ .

To understand the mechanism of enhanced surface-sensitive SHG response from individual R6G molecules on plasmonic nanohole arrays, we performed numerical simulations to calculate the field enhancement and local density of states (LDOS) at plasmonic hot spots on silver nanohole arrays. R6G is known to exhibit polarization-sensitive SHG emission, albeit at high sub-mM range of concentrations, in ensemble measurements at pump laser excitation of 780-800 nm.<sup>66</sup> We calculated the electric field intensity distribution in one unit cell of the nanostructure at both 800 nm and 400 nm wavelengths (Figures 5a, 5b). We observe that, while at 800 nm the structure does not have any strong resonances, at 400 nm the electric field is highly intensified at the edges of the nanohole. Molecules adsorbed close to these hot spots on the surface of the structure experience a significant increase in the local fields, which consequently enhances light-matter interactions at the location of these molecules. From Figure 5b, we observe that at 400 nm we have ~2.5 times electromagnetic field enhancement on the edges of the silver nanohole compared to the planar silver surface.

The intensified confinement of the electromagnetic field at the second harmonic resonance wavelength ( $\lambda = 400$  nm) increases LDOS at the outer rim of the nanoholes (Figures 5c, 5d). According to Fermi's golden rule, the increase in the LDOS leads to increase in the spontaneous emission rate of a dipole as follows:<sup>67,68</sup>  $\mathcal{Y}_{sp} = \frac{2\omega}{3\hbar\epsilon_0} |\mu|^2 \int_s \rho(\mathbf{r}, \omega) ds$ , where  $\rho(\mathbf{r}, \omega)$  is the LDOS,  $\hbar$  is the reduced Planck constant,  $\epsilon_0$  is the dielectric permittivity of free space, and  $\mu$  is the transition dipole moment of the emitter. The LDOS  $\rho(\mathbf{r}, \omega)$  was calculated using the equation:<sup>67,68</sup>  $\rho(\mathbf{r}, \omega) = \frac{2\omega}{\pi c^2} \{ \hat{n}_p \cdot \text{Im} \{ \text{Tr} [ \vec{G}(\mathbf{r}, \mathbf{r}) ] \cdot \hat{n}_p \} \}$ , where  $\hat{n}_p$  is the orientation of the transition dipole of the emitter,

1  
2  
3  $\vec{G}$  is the dyadic Green's function, and  $c$  is the speed of light in free space. Here, the function  $\vec{G}$   
4 takes in to account the interplay between the dipole of the emitter with its own local electric field.  
5  
6 Using the above equation, the LDOS was calculated at the center and at the outer rims of the  
7  
8 nanohole at  $\lambda = 400$  and  $800$  nm. In the FDTD simulations, an electric dipole emitter was  
9  
10 positioned at the center and at the edges of the nanohole, while its vertical location was  $2$  nm above  
11  
12 the surface of the sample. Figure 5e shows the LDOS enhancement at the center of the nanohole  
13  
14 (blue), and at the outer rim of the nanohole (red). The LDOS were calculated by averaging the  
15  
16 DOS of the dipole emitter over the three polarization directions. We observe that the LDOS is  
17  
18 significantly increased at the edges of the nanohole compared to the center. The spatial dependence  
19  
20 of the LDOS are shown in Figures 5c ( $\lambda = 800$  nm) and 5d ( $\lambda = 400$  nm). The LDOS and  
21  
22 consequently the spontaneous emission rate from an emitter increases by more than an order of  
23  
24 magnitude ( $\sim 12$  times) at the edges of the nanohole at the  $400$  nm wavelength (Figures 5c, 5d, and  
25  
26 5e). Therefore, our experimental and simulation results suggest that the increased confinement of  
27  
28 electromagnetic field at the hot spot locations near the R6G molecules lead to enhancement of  
29  
30 SHG emission on our device. Further, the confinement leads to enhanced light absorption and an  
31  
32 increase in the LDOS near the location of the R6G molecules, resulting in enhanced emission rate  
33  
34 of R6G at the wavelength of  $400$  nm. As seen in Figures 5b and 5d, the excitation electromagnetic  
35  
36 field enhancement at  $400$  nm of  $\sim 2.5$  on plasmonic hot spots in combination with the emission  
37  
38 enhancement of  $\sim 12$  in LDOS near the edges of the nanohole at  $400$  nm provides at least  $30$  times  
39  
40 total enhancement on the edges of the plasmonic silver nanohole substrate. We do not see any  
41  
42 SHG signal originating from R6G at  $10$   $\mu\text{M}$  concentration on the glass substrate, while on the  
43  
44 silver nanohole structure even at very dilute  $0.25$  nM concentration, we observe SHG emission  
45  
46 from single R6G molecules. As the SHG signal is proportional to the number of molecules ( $I_{SHG}$   
47  
48  
49  
50  
51  
52  
53  
54  
55  
56  
57  
58  
59  
60

1  
2  
3  $\propto N\beta$ , where  $N$  is the number of molecules and  $\beta$  is the hyperpolarizability of the molecule)<sup>69</sup>, the  
4 magnitude of SHG enhancement factor ( $EF$ ) on the plasmonic silver nanohole arrays is estimated  
5  
6  
7  
8 to be

9  
10  
11 
$$EF \sim I_{nanohole} N_{glass} / I_{nanohole} N_{nanohole} = 1.2 \times 10^6.$$

12 Figure 5g shows the proposed energy level scheme illustrating possible enhancement of the SHG  
13 signal from R6G molecules through two different mechanisms denoted as Schemes 1 and 2.  
14  
15 Scheme 2 shows the direct generation of SHG photons from R6G. Under 800 nm pulsed laser  
16 excitation source, R6G absorbs two photons to undergo an  $S_0 \rightarrow S_2$  transition. When R6G relaxes  
17 to its ground state, it will emit the SHG photon at 400 nm due to  $S_2 \rightarrow S_0$  transition. However, this  
18 transition process is weak, as it requires R6G concentrations above 1 mM (Figure S6). We believe  
19 the more dominant SHG emission pathway is likely arising through the configuration of Scheme  
20  
21  
22  
23  
24  
25  
26  
27  
28  
29  
30  
31  
32  
33  
34  
35  
36  
37  
38  
39  
40  
41  
42  
43  
44  
45  
46  
47  
48  
49  
50  
51  
52  
53  
54  
55  
56  
57  
58  
59  
60  
1. Therein, broad two photon fluorescence and plasmonic generation of photons at 530 nm from  
the silver nanohole array provides the pump excitation to populate the singlet state ( $S_1$ ) of R6G  
(Figure 5g). Finally, the two-photon absorption generates the SHG signal with a  $S_n \leftarrow S_1$  transition  
followed by a  $S_1 \leftarrow S_n$  SHG transition of the R6G molecule under 800 nm pulsed laser excitation.  
Similar mechanistic framework has been demonstrated for SHG emission in R6G through  
ensemble measurements.<sup>66</sup>

In summary, we demonstrate a unique SHG microscopy method for ultrasensitive  
collective plasmon enhanced SHG to achieve simultaneous visualization and 3D orientation  
imaging of individual R6G molecules using plasmonic silver nanohole arrays. These findings can  
be extended to detect and perform orientation imaging of single molecules in applications ranging  
from nanophotonics to complex biological systems.

## MATERIALS AND METHODS

### *Sample Fabrication.*

Nanoimprint lithography method was utilized to prepare the nanohole photonic structures.<sup>24, 42</sup> Briefly, UV-curable polymer (10  $\mu$ L) was dropped on a silica master mold (pitch = 350 nm) with nanopillar structure. After curing with a UV flood system with a power density of 105 mW/cm<sup>2</sup>, mirror image of the master mold structures were transferred to the supporting PET film to obtain nanohole array structures. Finally, 90 nm of Ag was deposited on the nanohole array PET film for the plasmonic devices.

### *Experimental Setup and Measurement of SHG Signals.*

The silver nanohole array plasmonic device dispersed with aqueous Rhodamine 6G (concentration  $\sim$  0.25 nM) was excited with a Ti-sapphire laser ( $f$  = 80 MHz,  $w_{\text{pulse}}$  = 100 fs,  $\lambda_{\text{pump}}$  = 800 nm) (Figure S9) using a 100x objective with numerical aperture of 1.4. The emitted light from the sample was separated by band-pass filters using the spectrometer at 380-400 nm for the SHG signal and 550-650 nm for the two-photon fluorescence signals. The average power at the sample was 10 mW. The obtained single molecule images were analyzed using a template matching algorithm described below to determine the molecular orientation in each image frame. The resolution of imaging system for SHG images was measured using a 100 nm gold nanoparticle and found to be 670 nm (Figure S10).

### *Template Matching Algorithm.*

To determine the depth and orientation of each molecule in the image and compare them to the simulated library of images, we employ a template matching algorithm<sup>70-72</sup> using the normalized cross correlation coefficient as a similarity measure. We first generate a set of

1  
2  
3 templates  $\{T_{\{\theta,\phi,z,s\}}(x,y)\}$  that uniformly samples the space of possible parameters of angles ( $\theta$   
4 and  $\phi$ ), scale in number of pixels ( $s$ ), and depth ( $z$ ) of the radiation pattern of a  
5 molecule/nanoparticle for the given wavelength of the experiment. We iterate over the  
6 experimentally generated image with each template, comparing each region in the image to the  
7 template using a MATLAB implementation of template matching, and the normalized cross  
8 correlation coefficient is given by  $NCCC_T(x,y) = \frac{\sum_{u,v} T(u,v) I(x+u,y+v)}{\sqrt{\sum_{u,v} T^2(u,v) \sum_{u,v} I^2(x+u,y+v)}}$  for each pixel location  
9  
10  
11  
12  
13  
14  
15  
16  
17  
18  
19  
20  
21  
22  
23  
24  
25  
26  
27  
28  
29  
30  
31  
32  
33  
34  
35  
36  
37  
38  
39  
40  
41  
42  
43  
44  
45  
46  
47  
48  
49  
50  
51  
52  
53  
54  
55  
56  
57  
58  
59  
60

( $x, y$ ), where  $I$  is the acquired image and ( $u, v$ ) are pixel locations in the template. This process yields a score for each template at each pixel location. The maximum score at each pixel is thresholded to remove weak matches which are not likely to correspond to the location of a molecule, producing a binary mask of candidate locations  $M(x,y) = I\left[\max_T\{NCCC_T(x,y)\} > \tau_{NCCC}\right]$ , where  $I$  is the indicator function. Regarding computational time required for template matching algorithm, typically running the algorithm for one 512 x 512-pixel image for given values of  $z$ , aperture, and  $n\_pixels$  (so we are only looking for  $\theta$  and  $\phi$ ) requires ~10-20 seconds. From there, the time scales linearly in  $z$ , aperture, and  $n\_pixels$ .

#### *Quantitative Assessment of Template Matching Algorithm.*

Theoretically, the only templates that are identical are those for which the vertical/axial angle,  $\theta$ , is zero. In this case, the imaged pattern will be isotropic, and therefore, changing  $\phi$  (azimuthal angle), which merely rotates the pattern about its center, will not result in any change. For any angle of  $\theta$  greater than zero, this will not be the case. However, although the templates will not be exactly the same, the difference may be small, especially for smaller angles of  $\theta$ .

1  
2  
3  
4  
5  
6  
7  
8  
9  
10  
11  
12  
13  
14  
15  
16  
17  
18  
19  
20  
21  
22  
23  
24  
25  
26  
27  
28  
29  
30  
31  
32  
33  
34  
35  
36  
37  
38  
39  
40  
41  
42  
43  
44  
45  
46  
47  
48  
49  
50  
51  
52  
53  
54  
55  
56  
57  
58  
59  
60

Seen in the figure (Figure S13 a) are the plots of the NCCC between templates. Recall from above that NCCC ranges from 0 - 1, with 1 being a perfect match. The first plot shows the pairwise difference between two templates with the same angle  $\theta$ , varied between 0 - 90 degrees (corresponding to the row index), but differing values of  $\phi$  (corresponding to column index). For one template,  $\phi$  was held to 0 degrees, while for the other, the angle  $\phi$  was varied from 0 - 360 degrees (corresponding to the column index). We can see that, for values of  $\theta < 30^\circ$ , changing  $\phi$ , or rotating the template, results in a negligible drop in NCCC. However, for values of  $\theta$  greater than 30 degrees, rotation of  $\phi$  results in an increasingly larger drop in NCCC. When  $\theta$  is nearly 90 degrees, the imaged pattern becomes symmetric to rotations of 180 degrees, which explains the increase in NCCC to 1 for  $\phi$  equal to 180 degrees and  $\theta$  equal to 90 degrees. The next figure (Figure S13b) shows the uniqueness of the templates by varying the angle  $\theta$  and keeping the angle  $\phi$  constant. Along the diagonal, the value of NCCC is 1, since  $\theta$  is the same for both templates. We can see that, as  $\theta$  increases beyond a threshold value ( $\theta \sim 30^\circ$ ), the templates become increasingly distinct from each other. However, for  $\theta < 30^\circ$ , the generated templates are not clearly distinct from each other (NCCC values close to 1). This leads to poor resolution in resolving angles for  $\theta < 30^\circ$ . On the other hand, when  $\theta > 30^\circ$ , the angular resolution for resolving the orientation of the molecule is  $\sim 6^\circ$ .

#### *Fluorescence Correlation Spectroscopy.*

FCS measurements of Rhodamine 6G were conducted on Alba FCS instruments (ISS, USA) based on a Nikon inverted confocal microscope equipped with 470 nm diode laser as single photon excitation source. Fluorescence intensity fluctuations were detected with an avalanche photodiode detector. All FCS data acquisition and fluorescence intensity temporal fluctuations were analysed using the VistaVision software package from ISS.

### *Numerical Simulations.*

#### *Calculation of the nonlinear transmission coefficient*

Lumerical FDTD (Finite Difference Time Domain) package was used for the simulations. The refractive index of silver and titanium were obtained from CRC data, and the refractive index of the polymer was 1.56. The mesh size was 2 nm throughout the simulation domain. Periodic boundary conditions was used in the  $x$  and  $y$  directions, and perfectly matched layers (PMLs) was used in the  $z$  direction. A high-power plane-wave was used to excite the nanostructure as the pump signal (normally incident from top) at 800 nm wavelength. The polarization of the excitation field was along the  $x$  direction. The transmitted power was collected using a plane frequency-domain field monitor which was placed below the nanohole array. The spectra were obtained through Fourier transform of the recorded electric fields.

#### *Calculation of the local density of states*

A simulation domain including several periods of the structure was used to calculate the LDOS. PML boundary conditions were utilized in  $x$ ,  $y$ , and  $z$  directions. The mesh size was 1 nm in the vicinity of the surface of the nanostructure and 5 nm in other areas. An electric dipole emitter was positioned at the center and at the edges of the nanohole. Its vertical location was at  $z = 2$  nm. For each point (either at the center or at the edge of the nanohole) and for each orientation of the dipole emitter (i.e.  $x$ ,  $y$  and  $z$ ) we calculated the Green's function, which is the electric field at  $\mathbf{r}$  generated by a dipole emitter located at  $\mathbf{r}_0$ , and used it to obtain the LDOS.

## **ASSOCIATED CONTENT**

### **Supporting Information**

The Supporting Information is available free of charge on the ACS Publications website at DOI:

1  
2  
3 SEM images of Nanohole Arrays, Optimum power calculation for the FCS experiment; calculating  
4 the confocal volume; detailed calculation of number of molecules within a single nanohole;  
5  
6 comparison of SHG and two photon fluorescence microscopy on glass, smooth metal and nanohole  
7  
8 array; template library for typical dipole oriented at certain angles; schematic of the experimental  
9  
10 set up; PSF of gold nanoparticle, histogram distribution of orientation angles, quantitative proof  
11  
12 of template matching algorithm.  
13  
14  
15

## 16 17 **AUTHOR INFORMATION**

### 18 19 **Corresponding Author**

20  
21 \*E-mail: mgartia@lsu.edu. Phone: +1225 5785900  
22  
23

### 24 **Author contributions**

25  
26 M.R.G. conceived and designed the experiments. S.P.S. performed the experiments. A.M. did the  
27  
28 FDTD simulations. B.C. wrote the template matching algorithm. M.R.G., S.P.S., B.C., A.M.  
29  
30 analyzed the data and wrote the manuscript. G.V. supervised the FDTD analysis. All the authors  
31  
32 provided input on the manuscript.  
33  
34

### 35 **Notes**

36  
37 The authors declare no competing financial interests.  
38  
39

## 40 **ACKNOWLEDGEMENTS**

41  
42 M.R.G. acknowledges LSU start-up fund and Louisiana Board of Regents Support Fund (RCS  
43  
44 Award Contract Number: LEQSF(2017-20)-RD-A-04). G.V. acknowledges support from NSF  
45  
46 (Award Number 1254934). SEM images were taken at LSU's Shared Instrumentation Facility  
47  
48 (SIF). SHG experiments were performed at Pennington Biomedical Research Center. We thank  
49  
50 Drs. David Burk, Logan Liu, and Mayandi Sivaguru for useful discussions.  
51  
52  
53  
54  
55  
56  
57

## REFERENCES

1. Hell, S. W.; Wichmann, J. Breaking the diffraction resolution limit by stimulated emission: stimulated-emission-depletion fluorescence microscopy. *Opt. Lett.* **1994**, *19*, 780-782.
2. Vicidomini, G.; Bianchini, P.; Diaspro, A. STED super-resolved microscopy. *Nat. Methods* **2018**, *15*, 173-182.
3. Betzig, E.; Patterson, G. H.; Sougrat, R.; Lindwasser, O. W.; Olenych, S.; Bonifacino, J. S.; Davidson, M. W.; Lippincott-Schwartz, J.; Hess, H. F. Imaging intracellular fluorescent proteins at nanometer resolution. *Science* **2006**, *313*, 1642-1645.
4. Rust, M. J.; Bates, M.; Zhuang, X., Sub-diffraction-limit imaging by stochastic optical reconstruction microscopy (STORM). *Nat. Methods* **2006**, *3*, 793-796.
5. Saleh, B. E.; Teich, M. C. Fundamentals of Photonics, John Wiley & Sons. Inc., Canada **1991**.
6. Terakawa, M.; Nedyalkov, N. N. Near-field optics for nanoprocessing. *Adv. Opt. Techn.* **2016**, *5*, 17-28.
7. Kauranen, M.; Zayats, A. V. Nonlinear plasmonics. *Nat. Photonics* **2012**, *6*, 737-748.
8. Butet, J.; Brevet, P.-F.; Martin, O. J. Optical second harmonic generation in plasmonic nanostructures: from fundamental principles to advanced applications. *ACS Nano* **2015**, *9*, 10545-10562.
9. Tran, R. J.; Sly, K. L.; Conboy, J. C. Applications of surface second harmonic generation in biological sensing. *Annu. Rev. Anal. Chem.* **2017**, *10*, 387-414.
10. Kim, M.-K.; Sim, H.; Yoon, S. J.; Gong, S.-H.; Ahn, C. W.; Cho, Y.-H.; Lee, Y.-H. Squeezing photons into a point-like space. *Nano Lett.* **2015**, *15*, 4102-4107.
11. Grinblat, G.; Rahmani, M.; Cortés, E.; Caldarola, M.; Comedi, D.; Maier, S. A.; Bragas, A. V. High-efficiency second harmonic generation from a single hybrid ZnO nanowire/Au plasmonic nano-oligomer. *Nano Lett.* **2014**, *14*, 6660-6665.
12. Liu, X.; Zhang, Q.; Chong, W. K.; Yip, J. N.; Wen, X.; Li, Z.; Wei, F.; Yu, G.; Xiong, Q.; Sum, T. C. Cooperative enhancement of second-harmonic generation from a single CdS nanobelt-hybrid plasmonic structure. *ACS Nano* **2015**, *9*, 5018-5026.
13. Timpu, F.; Hendricks, N. R.; Petrov, M.; Ni, S.; Renaut, C.; Wolf, H.; Isa, L.; Kivshar, Y.; Grange, R. Enhanced second-harmonic generation from sequential capillarity-assisted particle assembly of hybrid nanodimers. *Nano Lett.* **2017**, *17*, 5381-5388.
14. Aouani, H.; Rahmani, M.; Navarro-Cía, M.; Maier, S. A. Third-harmonic-upconversion enhancement from a single semiconductor nanoparticle coupled to a plasmonic antenna. *Nat. Nanotechnol.* **2014**, *9*, 290-294.

- 1  
2  
3 15. Metzger, B.; Hentschel, M.; Schumacher, T.; Lippitz, M.; Ye, X.; Murray, C. B.; Knabe,  
4 B.; Buse, K.; Giessen, H. Doubling the efficiency of third harmonic generation by positioning ITO  
5 nanocrystals into the hot-spot of plasmonic gap-antennas. *Nano Lett.* **2014**, *14*, 2867-2872.  
6  
7 16. Shen, S.; Meng, L.; Zhang, Y.; Han, J.; Ma, Z.; Hu, S.; He, Y.; Li, J.; Ren, B.; Shih, T.-M.  
8 Plasmon-enhanced second-harmonic generation nanorulers with ultrahigh sensitivities. *Nano Lett.*  
9 **2015**, *15*, 6716-6721.  
10  
11 17. Ghirardini, L.; Baudrion, A.-L.; Monticelli, M.; Petti, D.; Biagioni, P.; Duò, L.; Pellegrini,  
12 G.; Adam, P.-M.; Finazzi, M.; Celebrano, M. Plasmon-enhanced second harmonic sensing. *The J.*  
13 *Phys. Chem. C* **2018**, *122*, 11475-11481.  
14  
15 18. Thyagarajan, K.; Rivier, S.; Lovera, A.; Martin, O. J. Enhanced second-harmonic  
16 generation from double resonant plasmonic antennae. *Optics express* **2012**, *20*, 12860-12865.  
17  
18 19. Celebrano, M.; Wu, X.; Baselli, M.; Großmann, S.; Biagioni, P.; Locatelli, A.; De Angelis,  
19 C.; Cerullo, G.; Osellame, R.; Hecht, B. Mode matching in multiresonant plasmonic nanoantennas  
20 for enhanced second harmonic generation. *Nat. Nanotechnol.* **2015**, *10*, 412-417.  
21  
22 20. Muehlschlegel, P.; Eisler, H.-J.; Martin, O. J.; Hecht, B.; Pohl, D. Resonant optical  
23 antennas. *Science* **2005**, *308*, 1607-1609.  
24  
25 21. Ament, I.; Prasad, J.; Henkel, A.; Schmachtel, S.; Sonnichsen, C. Single unlabeled protein  
26 detection on individual plasmonic nanoparticles. *Nano Lett.* **2012**, *12*, 1092-1095.  
27  
28 22. Zhang, R.; Zhang, Y.; Dong, Z.; Jiang, S.; Zhang, C.; Chen, L.; Zhang, L.; Liao, Y.;  
29 Aizpurua, J.; Luo, Y.; Yang, J. L.; Hou, J. G. Chemical mapping of a single molecule by plasmon-  
30 enhanced Raman scattering. *Nature* **2013**, *498*, 82-86.  
31  
32 23. Chang, T. W.; Wang, X.; Hsiao, A.; Xu, Z.; Lin, G.; Gartia, M. R.; Liu, X.; Liu, G. L.  
33 Bifunctional Nano Lycurgus Cup Array Plasmonic Sensor for Colorimetric Sensing and  
34 Surface-Enhanced Raman Spectroscopy. *Adv. Opt. Mater.* **2015**, *3*, 1397-1404.  
35  
36 24. Mahigir, A.; Chang, T.-W.; Behnam, A.; Liu, G. L.; Gartia, M. R.; Veronis, G. Plasmonic  
37 nanohole array for enhancing the SERS signal of a single layer of graphene in water. *Sci. Rep.*  
38 **2017**, *7*, 14044.  
39  
40 25. Fu, B.; Flynn, J. D.; Isaacoff, B. P.; Rowland, D. J.; Biteen, J. S. Super-resolving the  
41 distance-dependent plasmon-enhanced fluorescence of single dye and fluorescent protein  
42 molecules. *J. Phys. Chem. C* **2015**, *119*, 19350-19358.  
43  
44 26. Li, J.-F.; Li, C.-Y.; Aroca, R. F. Plasmon-enhanced fluorescence spectroscopy. *Chem. Soc.*  
45 *Rev.* **2017**, *46*, 3962-3979.  
46  
47 27. Hou, W.; Cronin, S. B. A review of surface plasmon resonance-enhanced photocatalysis.  
48 *Adv. Funct. Mater.* **2013**, *23*, 1612-1619.  
49  
50 28. Maragò, O. M.; Jones, P. H.; Gucciardi, P. G.; Volpe, G.; Ferrari, A. C. Optical trapping  
51 and manipulation of nanostructures. *Nat. Nanotechnol.* **2013**, *8*, 807-819.  
52  
53  
54  
55  
56  
57  
58  
59  
60

- 1  
2  
3 29. Roxworthy, B. J.; Ko, K. D.; Kumar, A.; Fung, K. H.; Chow, E. K.; Liu, G. L.; Fang, N.  
4 X.; Toussaint Jr, K. C. Application of plasmonic bowtie nanoantenna arrays for optical trapping,  
5 stacking, and sorting. *Nano Lett.* **2012**, *12*, 796-801.  
6  
7 30. Senapati, D.; Singh, A. K.; Khan, S. A.; Senapati, T.; Ray, P. C. Probing real time gold  
8 nanostar formation process using two-photon scattering spectroscopy. *Chem. Phys. Lett.* **2011**,  
9 *504*, 46-51.  
10  
11 31. Singh, A. K.; Senapati, D.; Neely, A.; Kolawole, G.; Hawker, C.; Ray, P. C., Nonlinear  
12 optical properties of triangular silver nanomaterials. *Chem. Phys. Lett.* **2009**, *481*, 94-98.  
13  
14 32. Schön, P.; Bonod, N.; Devaux, E.; Wenger, J.; Rigneault, H.; Ebbesen, T. W.; Brasselet,  
15 S. Enhanced second-harmonic generation from individual metallic nanoapertures. *Opt. Lett.* **2010**,  
16 *35*, 4063-4065.  
17  
18 33. Belardini, A.; Larciprete, M. C.; Centini, M.; Fazio, E.; Sibilia, C.; Chiappe, D.; Martella,  
19 C.; Toma, A.; Giordano, M.; De Mongeot, F. B. Circular dichroism in the optical second-harmonic  
20 emission of curved gold metal nanowires. *Phys. Rev. Lett.* **2011**, *107*, 257401.  
21  
22 34. Linden, S.; Niesler, F.; Förstner, J.; Grynko, Y.; Meier, T.; Wegener, M. Collective effects  
23 in second-harmonic generation from split-ring-resonator arrays. *Phys. Rev. Lett.* **2012**, *109*,  
24 015502.  
25  
26 35. Kruk, S.; Weismann, M.; Bykov, A. Y.; Mamonov, E. A.; Kolmychek, I. A.; Murzina, T.;  
27 Panoiu, N. C.; Neshev, D. N.; Kivshar, Y. S. Enhanced magnetic second-harmonic generation from  
28 resonant metasurfaces. *ACS Photonics* **2015**, *2*, 1007-1012.  
29  
30 36. Canfield, B. K.; Husu, H.; Laukkanen, J.; Bai, B.; Kuittinen, M.; Turunen, J.; Kauranen,  
31 M. Local field asymmetry drives second-harmonic generation in noncentrosymmetric nanodimers.  
32 *Nano Lett.* **2007**, *7*, 1251-1255.  
33  
34 37. Zhang, Y.; Grady, N. K.; Ayala-Orozco, C.; Halas, N. J. Three-dimensional nanostructures  
35 as highly efficient generators of second harmonic light. *Nano Lett.* **2011**, *11*, 5519-5523.  
36  
37 38. Valev, V.; Silhanek, A.; Verellen, N.; Gillijns, W.; Van Dorpe, P.; Aktsipetrov, O.;  
38 Vandenbosch, G.; Moshchalkov, V.; Verbiest, T. Asymmetric optical second-harmonic generation  
39 from chiral G-shaped gold nanostructures. *Phys. Rev. Lett.* **2010**, *104*, 127401.  
40  
41 39. Valev, V.; Clercq, B.; Zheng, X.; Denkova, D.; Osley, E.; Vandendriessche, S.; Silhanek,  
42 A.; Volskiy, V.; Warburton, P.; Vandenbosch, G. The role of chiral local field enhancements below  
43 the resolution limit of Second Harmonic Generation microscopy. *Opt. Express* **2012**, *20*, 256-264.  
44  
45 40. Kujala, S.; Canfield, B. K.; Kauranen, M.; Svirko, Y.; Turunen, J. Multipolar analysis of  
46 second-harmonic radiation from gold nanoparticles. *Opt. Express* **2008**, *16*, 17196-17208.  
47  
48 41. Reichenbach, P.; Horneber, A.; Gollmer, D. A.; Hille, A.; Mihaljevic, J.; Schäfer, C.; Kern,  
49 D. P.; Meixner, A. J.; Zhang, D.; Fleischer, M., Nonlinear optical point light sources through field  
50 enhancement at metallic nanocones. *Opt. Express* **2014**, *22*, 15484-15501.  
51  
52  
53  
54  
55  
56  
57  
58  
59  
60

- 1  
2  
3 42. Gartia, M. R.; Hsiao, A.; Pokhriyal, A.; Seo, S.; Kulsharova, G.; Cunningham, B. T.; Bond,  
4 T. C.; Liu, G. L. Colorimetric plasmon resonance imaging using nano lycurgus cup arrays. *Adv.*  
5 *Opt. Mater.* **2013**, *1*, 68-76.  
6  
7 43. Forkey, J. N.; Quinlan, M. E.; Shaw, M. A.; Corrie, J. E.; Goldman, Y. E. Three-  
8 dimensional structural dynamics of myosin V by single-molecule fluorescence polarization.  
9 *Nature* **2003**, *422*, 399-404.  
10  
11 44. Toprak, E.; Enderlein, J.; Syed, S.; McKinney, S. A.; Petschek, R. G.; Ha, T.; Goldman,  
12 Y. E.; Selvin, P. R. Defocused orientation and position imaging (DOPI) of myosin V. *Proc. Natl.*  
13 *Acad. Sci. U.S.A.* **2006**, *103*, 6495-6499.  
14  
15 45. Ha, T.; Enderle, T.; Ogletree, D.; Chemla, D. S.; Selvin, P. R.; Weiss, S. Probing the  
16 interaction between two single molecules: fluorescence resonance energy transfer between a single  
17 donor and a single acceptor. *Proc. Natl. Acad. Sci. U.S.A.* **1996**, *93*, 6264-6268.  
18  
19 46. Eienthal, K. B. Second harmonic spectroscopy of aqueous nano-and microparticle  
20 interfaces. *Chem. Rev.* **2006**, *106*, 1462-1477.  
21  
22 47. Peterman, E. J.; Sosa, H.; Moerner, W. Single-molecule fluorescence spectroscopy and  
23 microscopy of biomolecular motors. *Annu. Rev. Phys. Chem.* **2004**, *55*, 79-96.  
24  
25 48. Andoy, N. M.; Zhou, X.; Choudhary, E.; Shen, H.; Liu, G.; Chen, P. Single-molecule  
26 catalysis mapping quantifies site-specific activity and uncovers radial activity gradient on single  
27 2D nanocrystals. *J. Am. Chem. Soc.* **2013**, *135*, 1845-1852.  
28  
29 49. Ishitobi, H.; Nakamura, I.; Hayazawa, N.; Sekkat, Z.; Kawata, S. Orientational imaging of  
30 single molecules by using azimuthal and radial polarizations. *J. Phys. Chem. B* **2010**, *114*, 2565-  
31 2571.  
32  
33 50. Ha, T.; Laurence, T. A.; Chemla, D. S.; Weiss, S. Polarization spectroscopy of single  
34 fluorescent molecules. *J. Phys. Chem. B* **1999**, *103*, 6839-6850.  
35  
36 51. Patra, D.; Gregor, I.; Enderlein, J. Image analysis of defocused single-molecule images for  
37 three-dimensional molecule orientation studies. *J. Phys. Chem. A* **2004**, *108*, 6836-6841.  
38  
39 52. Lieb, M. A.; Zavislan, J. M.; Novotny, L. Single-molecule orientations determined by  
40 direct emission pattern imaging. *J. Opt. Soc. Am. B* **2004**, *21*, 1210-1215.  
41  
42 53. Backlund, M. P.; Lew, M. D.; Backer, A. S.; Sahl, S. J.; Grover, G.; Agrawal, A.; Piestun,  
43 R.; Moerner, W. Simultaneous, accurate measurement of the 3D position and orientation of single  
44 molecules. *Proc. Natl. Acad. Sci. U.S.A.* **2012**, *109*, 19087-19092.  
45  
46 54. Sick, B.; Hecht, B.; Novotny, L. Orientational imaging of single molecules by annular  
47 illumination. *Phys. Rev. Lett.* **2000**, *85*, 4482-4485.  
48  
49 55. Han, F.; Guan, Z.; Tan, T. S.; Xu, Q.-H. Size-dependent two-photon excitation  
50 photoluminescence enhancement in coupled noble-metal nanoparticles. *ACS Appl. Mater.*  
51 *Interfaces* **2012**, *4*, 4746-4751.  
52  
53  
54  
55  
56  
57  
58  
59  
60

- 1  
2  
3 56. Zhou, R.; Lu, H.; Liu, X.; Gong, Y.; Mao, D. Second-harmonic generation from a periodic  
4 array of noncentrosymmetric nanoholes. *J. Opt. Soc. Am. B* **2010**, *27*, 2405-2409.  
5  
6 57. Hou, R.; Shynkar, V.; Lafargue, C.; Kolkowski, R.; Zyss, J.; Lagugné-Labarthe, F. Second  
7 harmonic generation from gold meta-molecules with three-fold symmetry. *Phys. Chem. Chem.*  
8 *Phys.* **2016**, *18*, 7956-7965.  
9  
10 58. Taflove, A.; Hagness, S. C. Computational Electrodynamics: The Finite-Difference Time-  
11 Domain Method, 2<sup>nd</sup> ed. Artech House, **2000**.  
12  
13 59. Punj, D.; Mivelle, M.; Moparthi, S. B.; Van Zanten, T. S.; Rigneault, H.; Van Hulst, N. F.;  
14 García-Parajó, M. F.; Wenger, J. A plasmonic 'antenna-in-box' platform for enhanced single-  
15 molecule analysis at micromolar concentrations. *Nat. Nanotech.* **2013**, *8*, 512-516.  
16  
17 60. Rigneault, H.; Capoulade, J.; Dintinger, J.; Wenger, J.; Bonod, N.; Popov, E.; Ebbesen, T.  
18 W.; Lenne, P.-F. Enhancement of single-molecule fluorescence detection in subwavelength  
19 apertures. *Phys. Rev. Lett.* **2005**, *95*, 117401.  
20  
21 61. Magde, D.; Wong, R.; Seybold, P. G., Fluorescence Quantum Yields and Their Relation to  
22 Lifetimes of Rhodamine 6G and Fluorescein in Nine Solvents: Improved Absolute Standards for  
23 Quantum Yields. *Photochem. Photobiol.* **2002**, *75*, 327-334.  
24  
25 62. Gartia, M. R.; Eichorst, J. P.; Clegg, R. M.; Logan Liu, G. Lifetime imaging of radiative and  
26 non-radiative fluorescence decays on nanoplasmonic surface. *Appl. Phys. Lett.* **2012**, *101*, 023118.  
27  
28 63. Pantazis, P.; Maloney, J.; Wu, D.; Fraser, S. E. Second harmonic generating (SHG) nanoprobe  
29 for in vivo imaging. *Proc. Natl. Acad. Sci. U.S.A.* **2010**, *107*, 14535-14540.  
30  
31 64. Turley, H. K.; Hu, Z.; Jensen, L.; Camden, J. P. Surface-Enhanced Resonance Hyper-Raman  
32 Scattering Elucidates the Molecular Orientation of Rhodamine 6G on Silver Colloids *J. Phys.*  
33 *Chem. Lett.* **2017**, *8*, 1819-1823.  
34  
35 65. Kikteva, T.; Star, D.; Zhao, Z.; Tammy L. Baisley, T. L.; Leach, G. W. Molecular Orientation,  
36 Aggregation, and Order in Rhodamine Films at the Fused Silica/Air Interface. *J. Phys. Chem. B*  
37 **1999**, *103*, 1124-1133.  
38  
39 66. Fedoseeva, M.; Letrun, R.; Vauthey, E. Excited-state dynamics of rhodamine 6G in  
40 aqueous solution and at the dodecane/water interface. *J. Phys. Chem. B* **2014**, *118*, 5184-5193.  
41  
42 67. Novotny, L.; Hecht, B. Principles of Nano-optics. Cambridge university press: **2012**.  
43  
44 68. Akselrod, G. M.; Argyropoulos, C.; Hoang, T. B.; Ciraci, C.; Fang, C.; Huang, J.; Smith,  
45 D. R.; Mikkelsen, M. H. Probing the mechanisms of large Purcell enhancement in plasmonic  
46 nanoantennas. *Nat. Photonics* **2014**, *8*, 835-840.  
47  
48 69. Campagnola, P. J.; Loew, L. M. Second-harmonic imaging microscopy for visualizing  
49 biomolecular arrays in cells, tissues and organisms. *Nat. Biotechnol.* **2003**, *21*, 1356-1360.  
50  
51  
52  
53  
54  
55  
56  
57  
58  
59  
60

- 1  
2  
3 70. Kenue, S. K. Lanelok: Detection of lane boundaries and vehicle tracking using image-  
4 processing techniques-part II: Template matching algorithms, SPIE Conference on Mobile Robots,  
5 **1989**, 1195, 234-245.  
6  
7 71. Prasanna, K.; Krishnan, V. Efficient parallel algorithms for image template matching on  
8 hypercube SIMD machines. *IEEE Trans. Pattern Anal. Mach. Intell.* **1989**, 11, 665-669.  
9  
10 72. Wagner, R.; Galiana, H. Evaluation of three template matching algorithms for registering  
11 images of the eye. *IEEE Trans. Biomed. Eng.* **1992**, 39, 1313-1319.  
12  
13  
14  
15  
16  
17  
18  
19  
20  
21  
22  
23  
24  
25  
26  
27  
28  
29  
30  
31  
32  
33  
34  
35  
36  
37  
38  
39  
40  
41  
42  
43  
44  
45  
46  
47  
48  
49  
50  
51  
52  
53  
54  
55  
56  
57  
58  
59  
60

## FIGURES

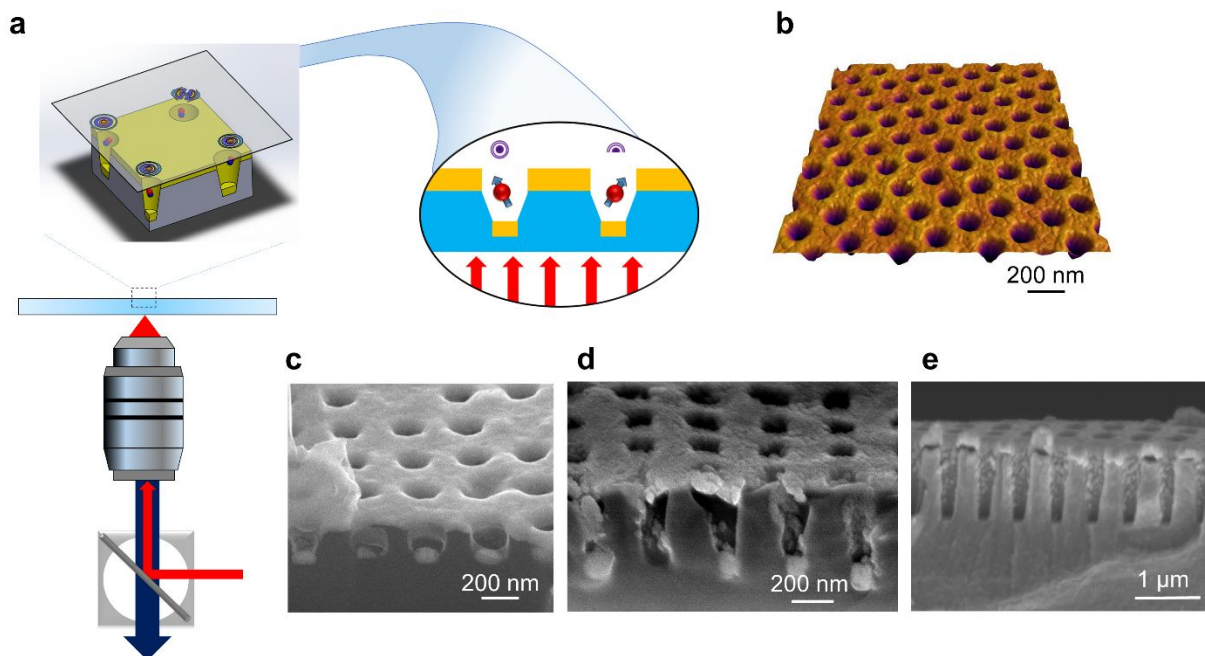


**Figure 1.** (a) Schematic of the SHG experiments showing the inverted microscopy set-up and the position of the sample. The zoomed in image shows the molecule as a dipole emitter within individual silver nanoholes. (b) AFM image of the fabricated structures showing the periodic array of nanoholes. Cross-sectional SEM image of the device showing the device with hole depth of (c) 250 nm, (d) 500 nm, and (e) 1,000 nm.

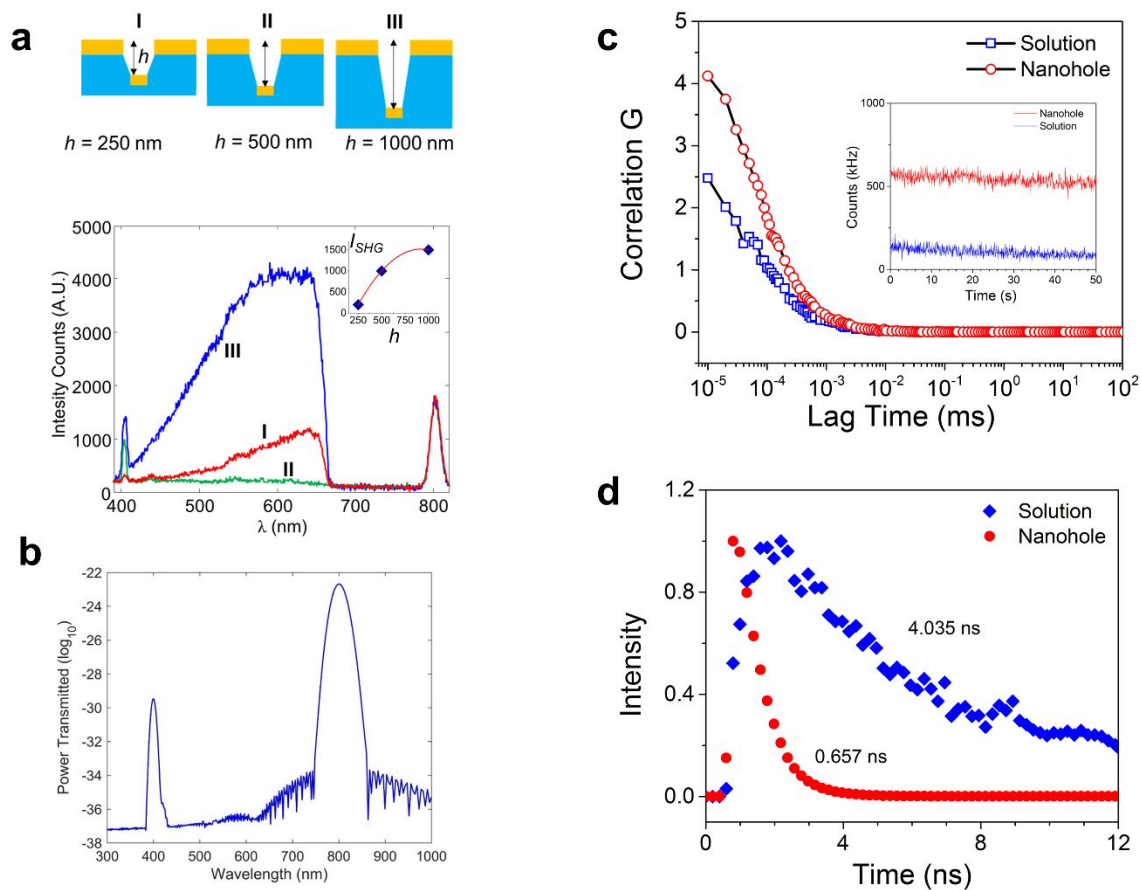


**Figure 2.** (a) Schematic of the nanohole device with 3 different hole depths on which SHG experiments were performed. Experimental SHG spectra generated by the nanohole devices with different hole depths. The inset shows the variation of SHG intensity at 400 nm with the hole depths. (b) Calculated transmission coefficient through the nanohole array as a function of wavelength. A high-power excitation plane wave with 800 nm wavelength is used to excite the structure. The second harmonic resonance of the structure is at 400 nm. (c) Fluorescence correlation functions measured for R6G in a solution and on the silver nanohole structure ( $h = 500$  nm). The inset shows the corresponding fluorescence time traces. (d) Fluorescence lifetime analysis of R6G with and without the nanohole structure.

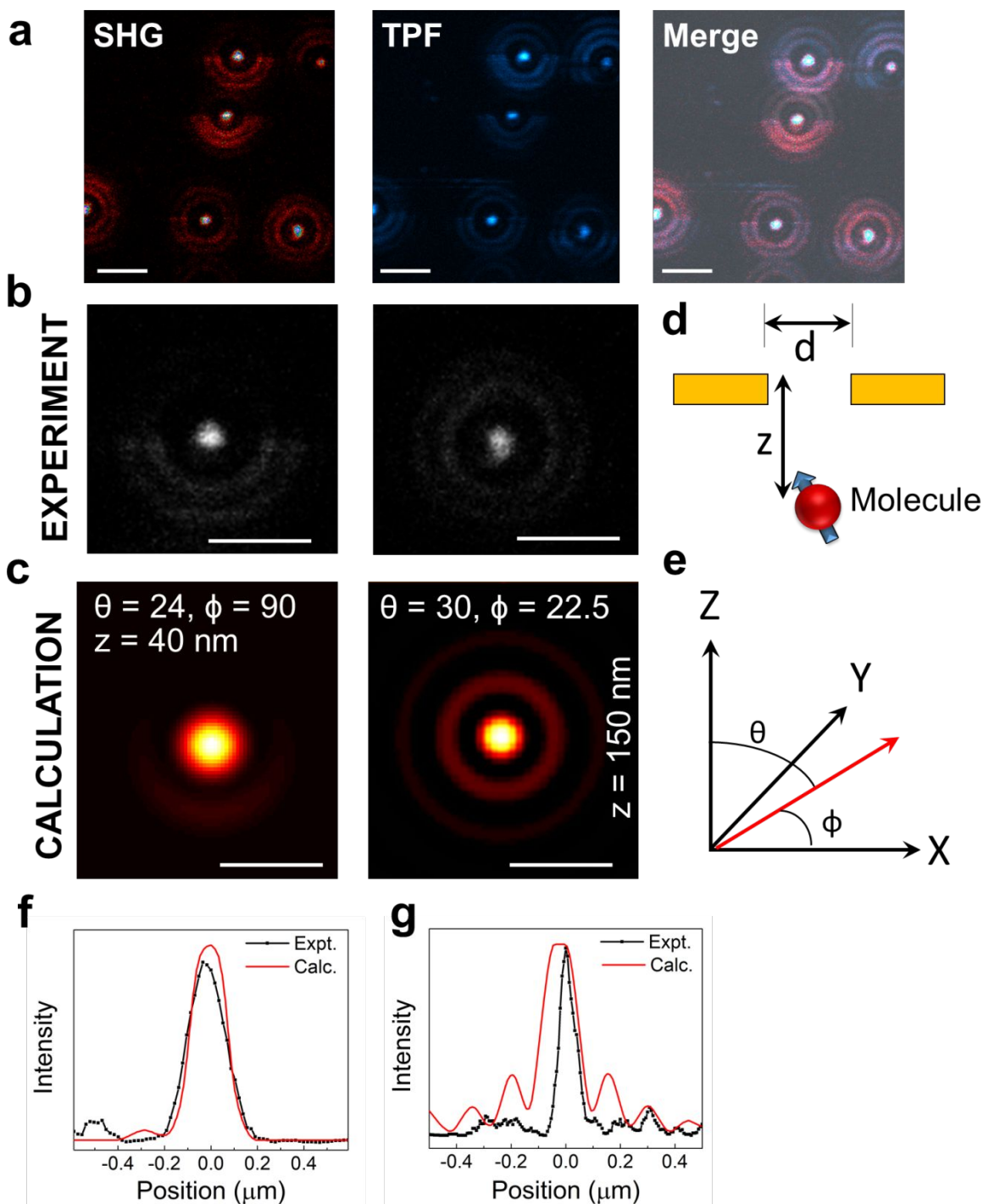


**Figure 3.** (a) SHG, two-photon fluorescence (TPF), and merged images of single molecule rhodamine 6G (R6G) on the nanohole structure. Representative images of single R6G molecules

1  
2  
3 at a depth of  $z = 40$  nm and  $z = 150$  nm from the (b) experimental data and (c) the corresponding  
4 simulation results of the dipole emission patterns through the aperture (nanohole structure); (d, e)  
5 the schematic depiction of nanohole aperture, distance of the molecule from the surface and the  
6 coordinate system where the  $Z$  is the optical axis,  $\theta$  is the polar angle measured with respect to  $Z$ ,  
7 and  $\phi$  is the azimuthal angle measured with respect to the  $Z$  axis. Comparison of experimental and  
8 simulation results shown in Figures 3b and 3c for two different positions: (f)  $z = 40$  nm (g)  $z = 150$   
9 nm. The scale bars in all images correspond to 500 nm.  
10  
11  
12  
13  
14  
15  
16  
17  
18  
19  
20  
21  
22  
23  
24  
25  
26  
27  
28  
29  
30  
31  
32  
33  
34  
35  
36  
37  
38  
39  
40  
41  
42  
43  
44  
45  
46  
47  
48  
49  
50  
51  
52  
53  
54  
55  
56  
57  
58  
59  
60

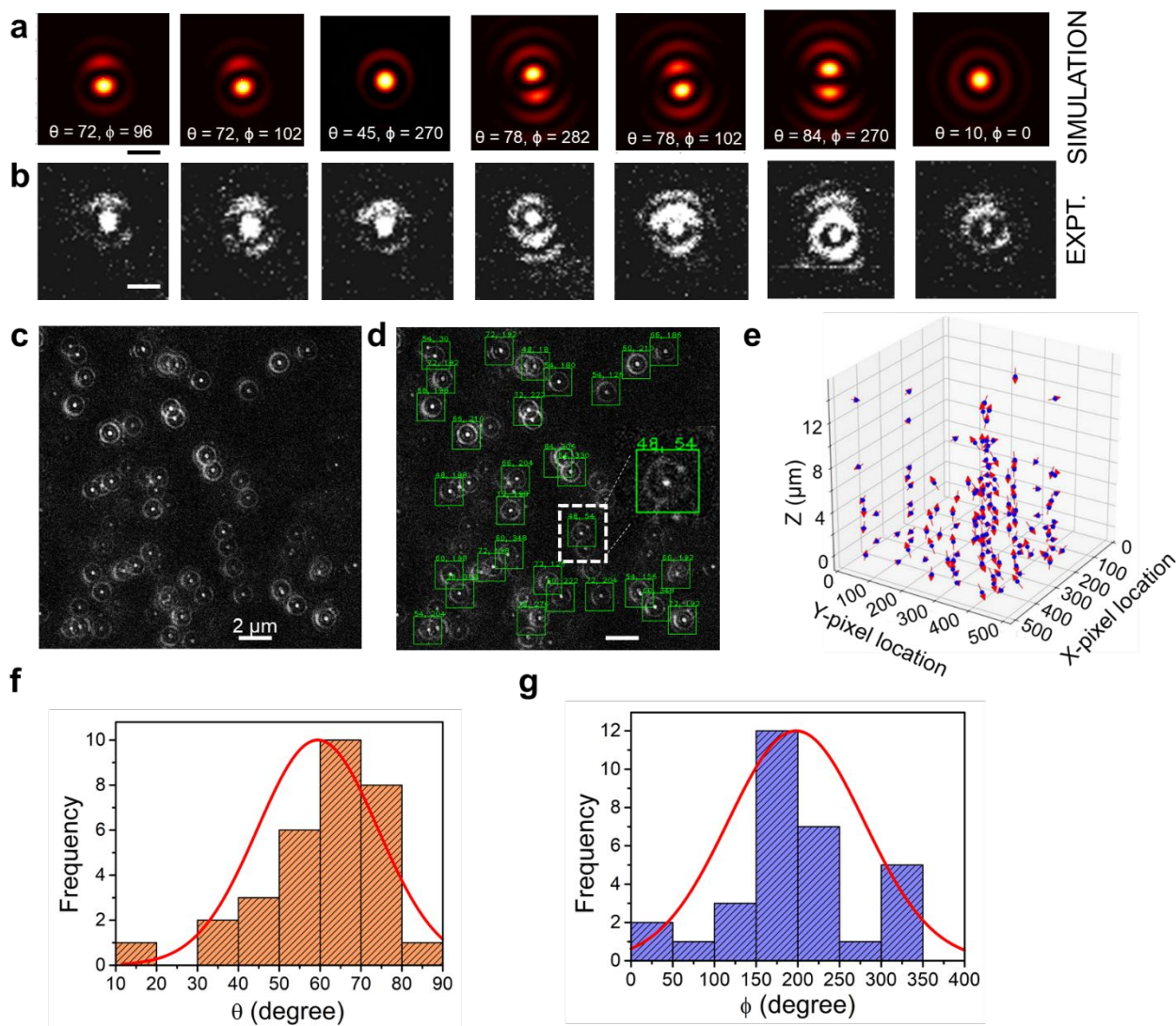


**Figure 4.** Template matching algorithm to find the orientation of the molecule in 3D. (a) Simulated images at different  $\theta$  and  $\phi$  at fixed aperture (b) Examples of corresponding experimental SHG images with matching patterns simulated in Figure 4a. The scale bar in Figures 4a and 4b corresponds to 500 nm. (c) Representative SHG images of R6G molecules on the nanohole substrate. (d) Values of  $\theta$  and  $\phi$  indicated in the image obtained by the template matching algorithm for Figure 4c. The scale bar in Figures 4c and 4d corresponds to  $2\ \mu\text{m}$ . (e) 3D mapping of single molecule with its orientation predicted by the template matching algorithm; the blue dot represents

the position of the molecule and the resultant angles of  $\theta$  and  $\phi$  are denoted by the red arrows.

Histogram distribution of orientation angles in (f) polar direction,  $\theta$ , (g) azimuthal direction,  $\phi$ .

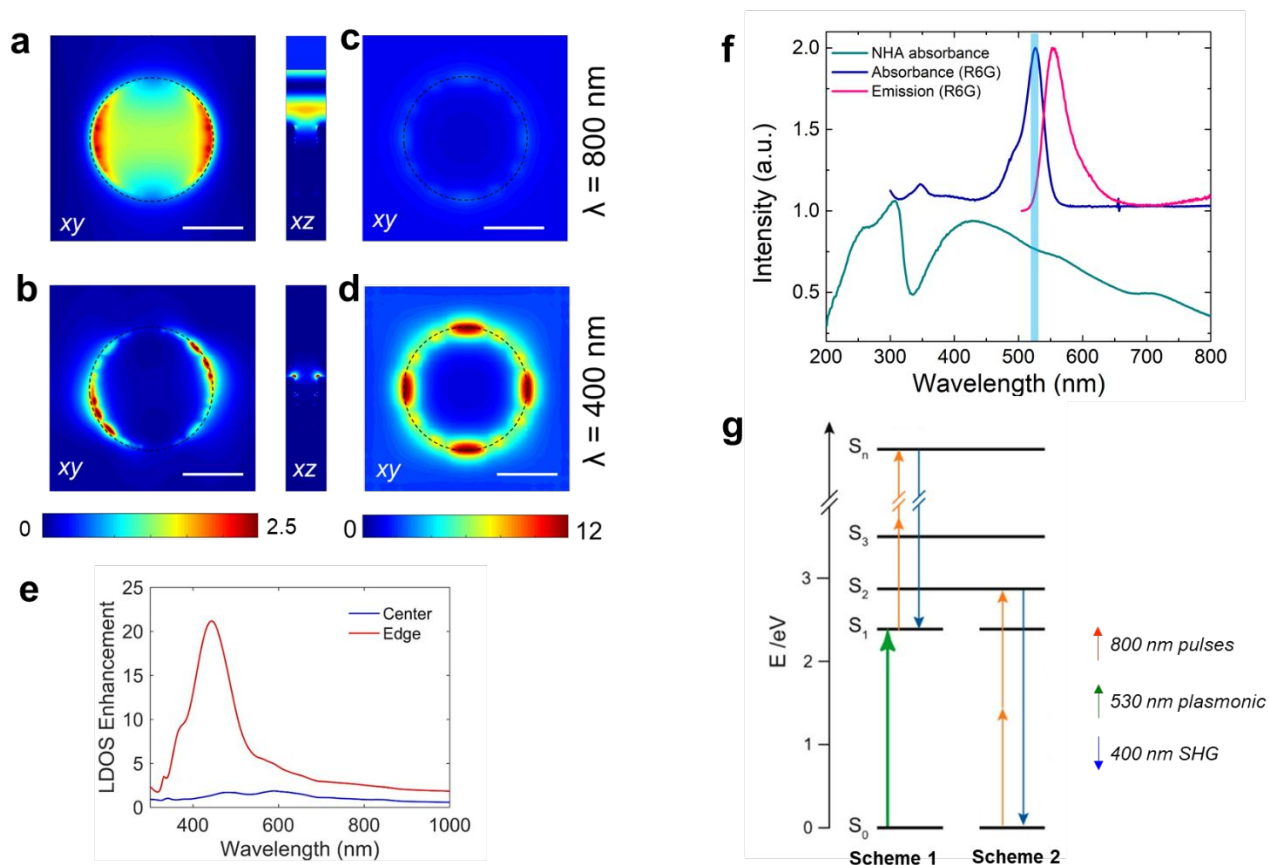


**Figure 5.** Electric field intensity calculated at (a)  $\lambda = 800$  nm and plotted in the  $xy$  plane (top view of the nanohole device). The image on the right shows the electric field distribution in the  $xz$  plane (side view or along the cross section of the nanohole device) calculated at  $\lambda = 800$  nm. (b) The corresponding electric field distribution in the  $xy$  and  $xz$  planes calculated at  $\lambda = 400$  nm. Local density of photonic states (LDOS) enhancement map calculated on the surface of the nanohole array at (c)  $\lambda = 800$  nm, and (d)  $\lambda = 400$  nm. (e) LDOS enhancement variation with wavelength calculated at the center of the nanohole (blue), and at the edges of the nanohole. (f) Absorbance of the nanohole array (NHA) device showing the plasmonic resonance of the structure with  $h = 1000$

1  
2  
3 nm. The absorption and emission spectra of R6G are also plotted showing the plasmonic –R6G  
4  
5 molecule interaction. (g) Jablonski diagram showing the probable energy transitions scheme for  
6  
7 the plasmon-enhanced SHG signal generation from single R6G molecules.  
8  
9  
10  
11  
12  
13  
14  
15  
16  
17  
18  
19  
20  
21  
22  
23  
24  
25  
26  
27  
28  
29  
30  
31  
32  
33  
34  
35  
36  
37  
38  
39  
40  
41  
42  
43  
44  
45  
46  
47  
48  
49  
50  
51  
52  
53  
54  
55  
56  
57  
58  
59  
60

## TOC Graphic

